A&A 641, A89 (2020)
https://doi.org/10.1051/0004-6361/202038303

Astronomy & Astrophysics

Geometry of the X-ray source 1H 0707–495

Michał Szanecki[1], Andrzej Niedźwiecki[2], Chris Done[3], Łukasz Klepczarek[2], Piotr Lubiński[4], and Misaki Mizumoto[5,6,3]

[1] Nicolaus Copernicus Astronomical Center, Polish Academy of Sciences, Bartycka 18, 00-716 Warszawa, Poland
e-mail: mitsza@camk.edu.pl
[2] Faculty of Physics and Applied Informatics, Łódź University, Pomorska 149/153, 90-236 Łódź, Poland
[3] Centre for Extragalactic Astronomy, Department of Physics, University of Durham, South Road, Durham DH1 3LE, UK
[4] Institute of Physics, University of Zielona Góra, Licealna 9, 65-417 Zielona Góra, Poland
[5] Hakubi Center, Kyoto University, Yoshida-honmachi, Sakyo-ku, Kyoto 606-8501, Japan
[6] Department of Astronomy, Kyoto University, Kitashirakawa-oiwakecho, Sakyo-ku, Kyoto 606-8502, Japan

Received 30 April 2020 / Accepted 29 June 2020

ABSTRACT

Aims. We investigate the constraints on the size and location of the X-ray source in 1H 0707–495 determined from the shape of the relativistically smeared reflection from the accretion disc.
Methods. We developed a new code to model an extended X-ray source and we applied this code to all archival XMM observations of 1H 0707–495.
Results. In contrast to earlier works we find that the relativistic reflection in this source is not consistent with an extended uniform corona. Instead, we find that the X-ray source must be very compact, at most a gravitational radius in size, and located at most a few gravitational radii from the black-hole horizon. A uniform extended corona produces an emissivity that is similar to a twice-broken power-law, but the inner emissivity is fixed by the source geometry rather than being a free parameter. In 1H0707–495, the reflection from the inner disc is much stronger than expected for a uniformly extended source. Including the effect of ionised absorption from the wind does not change this conclusion, but including scattered emission (and more complex absorption) from the wind can dramatically change the reflection parameters.

Key words. accretion, accretion disks – black hole physics – galaxies: Seyfert – X-rays: individuals: 1H 0707–495

1. Introduction

1H 0707–495 is a narrow-line Seyfert 1 galaxy well known for a sharp drop in its spectrum around 7 keV (Boller et al. 2002). This spectral feature can be imprinted either by an absorbing material on our line of sight (e.g. Tanaka et al. 2004; Done et al. 2007; Hagino et al. 2016; Mizumoto et al. 2019) or by irradiation of an accretion disc (e.g. Fabian et al. 2009; Zoghbi et al. 2010; Dauser et al. 2012). We consider the latter and we study constraints on the size and location of the X-ray source, which can be derived under this spectral interpretation.

Relativistic reflection spectroscopy is an important tool to constrain the geometry of accretion flows in their inner parts (e.g. Tanaka et al. 1995; Fabian & Ross 2010; Brenneman 2013). Two approximations are commonly used for such studies to simplify the model parametrisation and computations. First, in so-called lamppost geometry, irradiation of the disc surface by a point-like source is assumed (Martocchia & Matt 1996, and many later works). This allows us to estimate the distance of the X-ray source, but not its size. Secondly, even more often a phenomenological radial emissivity, typically a power law, is assumed, without any explicit assumption about the X-ray source. In this case, departures of the estimated emissivity from the dissipation profile of a Keplerian disc indicate that effects of the source-to-disc radiation transfer may be involved in shaping a reflection spectrum. Then, fitted emissivity can be used to infer the source geometry.

Such an approach was proposed by Wilkins & Fabian (2012, hereafter WF12). These authors showed the apparent similarity between an empirical, double-broken, power-law radial emissivity and the actual emissivity of the disc irradiated by an extended source, and used this to find the time averaged size of the X-ray source in 1H 0707–495 of about 30 gravitational radii. Then, Wilkins et al. (2014, hereafter W14) used spectra binned by the flux to show that the inferred outer break radius of the emissivity decreases with flux, and again compared these emissivities with their extended source illumination to claim that the size of the extended X-ray source decreases with decreasing source luminosity.

To gauge the accuracy of their approach, we develop in this work a similar relativistic reflection model with an extended X-ray source. However, rather than limiting our study to the qualitative comparison of this model with empirical emissivities (as WF12 and W14 did), we use this model directly to carry out a spectral description of 1H 0707–495. A part of this work addresses WF12 and W14, therefore, we adopt their data reduction method and assumptions about the X-ray source, and we use the same rest-frame reflection model rather than the newer models now available.

We also discuss in detail the reflection strength, which is the normalisation of the observed reflection with respect to the direct spectral component from the X-ray source. This quantity is strictly determined for a given geometry (see e.g. Dauser et al. 2014) and then gives a crucial test of the self-consistency of a model. However, this important constraint is often neglected in the X-ray data analysis. This concerns, in particular, all relativistic reflection models of 1H 0707–495 noted above.

Finally, evidence for a blue-shifted, photo-ionised outflow in 1H 0707–495 was reported by Dauser et al. (2012), Hagino et al. (2016), and Kosec et al. (2018). We take these results into account and investigate how the presence of such a blue-shifted absorber affects the fitted parameters of our reflection model.

2. Data reduction

We considered 15 *XMM-Newton* (Jansen et al. 2001) observations of 1H 0707–495 between 2000 and 2011 with an exposure time longer than 10 ks, (see e.g. Table 1 in Hagino et al. 2016). The 15 spectra from the EPIC pn detector (Strüder et al. 2001) were extracted using the *XMM-Newton* Science Analysis Software (SAS) version 17.0.0, and the current calibration file released on 29 March 2019. The data were reduced separately for each observation. We applied the standard selection criteria with the `PATTERN` ≤4 condition and excluding periods with the 10–12 keV background rate above 0.4 counts per second. The source spectra were extracted for a circular region that is 60 arcsec in diameter. For the background spectra, we found the optimal circular region via the `ebkgreg` tool, which was typically chosen to be a region of about 120 arcsec in diameter. The response files for each spectrum were generated with the `rmfgen`[1] and `arfgen`[2] tools.

The observation performed in January 2011 (Obs. ID 0554710801) caught the source in an extremely low state (Fabian et al. 2012) and is treated separately in this work; we refer to this as a very low (VL) state. The remaining 14 observations were combined to build the spectra of three non-overlapping count rate intervals that have <4, 4–6, and 6–10 counts s^{-1} (in the 0.2–10 keV energy range), which we refer to as the low (L), medium (M), and high (H) state, respectively. This selection of flux-resolved spectra is similar to that used in W14 and it is based on the assumption that the state of the X-ray source is determined by the X-ray flux. Spectral differences between these spectra could be then used to verify whether systematic changes of the source geometry correspond to the change of the observed flux.

Light curves of 1H 0707–495 with the time bin equal to 100 s were extracted with the same size of the source and background regions as the spectra and corrected with the `epiclccorr` tool. Using the light curves we created good time intervals (GTI) files for each of the 14 observations, applying the above count rate criteria. The spectra selected by count rate were extracted using these GTI files, with appropriate response files. Finally, the spectra for each count rate range were summed with the `epicspeccombine` tool. The resulting spectra have total exposure times of 64.5 (VL), 313.5 (L), 318 (M), and 237.8 (H) ks.

Our selection criteria for flux-resolved spectra are almost the same as those applied in W14, except for the energy range used for spectral selection, which in our case is slightly larger than the 0.3–10 keV range used in that work. Our extracted light curves are then essentially the same as those shown in Fig. 1 of W14, except for a slightly larger (by about 0.5 counts s^{-1}) amplitude of our light curves.

Following W14, we considered the 1.1–10 keV range. For spectral binning we adopted two approaches. For our basic version of the binning, referred to as binning (1), we used the `specgroup` tool of SAS with the minimal signal-to-noise ratio for each channel set to 5 and the oversample parameter set to 3. To address the results of W14, we used also binning (2) following their procedure, that is via the `grppha` tool of the `HEASOFT` package, with the condition of having at least 25 counts in each spectral bin. We note large differences regarding assessments of the agreement of the considered spectral model with the spectra binned using procedures (1) and (2).

[1] `xmm-tools.cosmos.esa.int/external/sas/current/doc/rmfgen`
[2] `xmm-tools.cosmos.esa.int/external/sas/current/doc/arfgen`

3. Model

The model developed in this work, referred to as `reflkerr_elp` (for extended lamppost), closely follows the lamppost model `reflkerr_lp` of Niedźwiecki et al. (2019), except for taking into account the spatial extent and rotation of an X-ray source, instead of treating it as point-like and static (lamppost). We consider a Keplerian disc in the Kerr metric, irradiated by a cylindrical corona with radius r_c, located symmetrically around the black-hole rotation axis between a lower height $h_{\rm min}$ and upper height $h_{\rm max}$. The inclination angle of a distant observer is denoted by i. All length scales r, h are in units of the gravitational radius, $R_g = GM/c^2$. All the results presented below are for $a = 0.998$. We assume that the corona is uniform, that is its rest-frame emissivity is constant in Boyer-Lindquist coordinates.

The finite size of the corona means that we should also include its dynamics. We assume that the corona co-rotates with the disc, that is the angular velocity of the corona at (r, θ) equals the Keplerian velocity, $\Omega_{\rm K}(\rho)$, where $\rho = r\sin\theta$. For $\rho < r_{\rm ISCO}$ we assume rigid rotation with $\Omega_{\rm K}(r_{\rm ISCO})$, where $r_{\rm ISCO}$ is the radius of the innermost stable circular orbit.

The inner radius of the disc is denoted by $r_{\rm in}$ and we assume that $r_{\rm in} \geq r_{\rm ISCO}$. 1H 0707–495 may be accreting at a rate close to the Eddington limit (see e.g. Done & Jin 2016), which may mean that the region of the flow at $r < r_{\rm ISCO}$ is optically thick so it can contribute to the observed reflection (Reynolds & Begelman 1997). This effect is not included in all previous studies of this object. We check that this is negligible in our models, all of which have extreme a, and inclination angles $i \simeq (40–50)°$.

Our computation of the fluxes of the X-ray radiation, either reaching the distant observer directly or illuminating the disc surface, strictly follows the model of Niedźwiecki & Życki (2008, hereafter NZ08); see Appendix A for technical details of our `xspec` implementation and comparison with similar computations.

To compute the observed reflected component, we apply the procedure used in the `reflkerr_lp` model, with `reflionx` (Ross & Fabian 2005) used for the rest-frame reflection. In Sects. 5.1 and 5.4 we apply the `reflkerr` model (Niedźwiecki et al. 2019), in which we also use `reflionx` for the rest-frame reflection (instead of `hreflect` originally used in `reflkerr`). In our fitting procedure, we use a free normalisation of the reflection component, which allows us to compare our results with previous works. We scale the reflection normalisation by $\mathcal{R}$, where $\mathcal{R} = 1$ corresponds to the actual normalisation for a given geometry. For the discussion below we also define the reflection strength, $\mathcal{R}_{\rm obs}$, defined here as the ratio of the observed reflected and direct fluxes in the 20–30 keV range.

Figure 1 illustrates changes of the reflection spectra corresponding to the contraction of the X-ray source in the vicinity of the black-hole horizon. We start with the magenta line showing a fairly large and thick corona, where $h_{\rm max} = r_c = 30$ and $h_{\rm min} = 0$. We successively shrink $h_{\rm max} = r_c$ to 8 (blue) 3 (green) 2 (red), and 1.3 (black). The increase in relativistic broadening for smaller sizes is clear, as is the increasing $\mathcal{R}_{\rm obs}$. The latter results

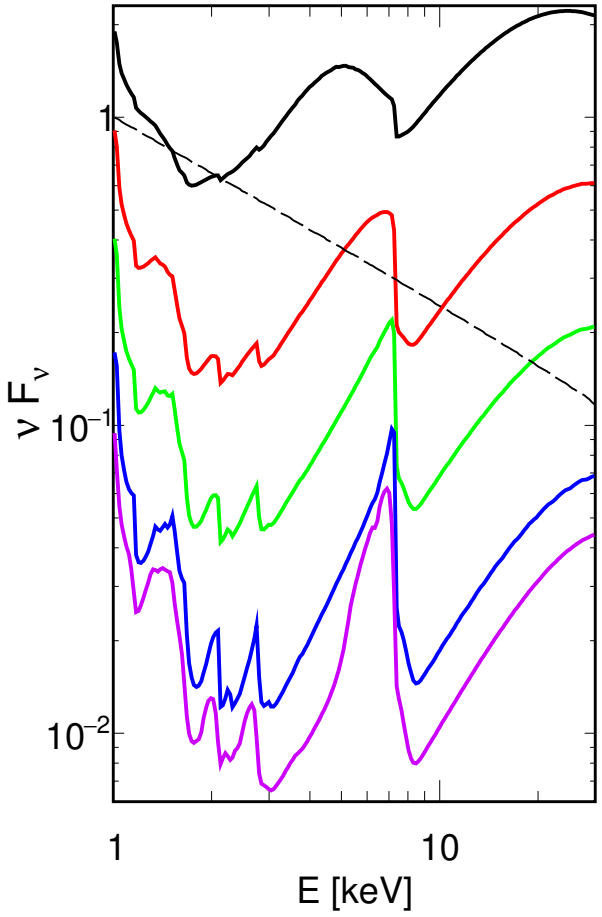

Fig. 1. Illustration of changes of the reflection spectrum resulting from the contraction of the X-ray source, described by the decrease of both $h_{\rm max}$ and $r_{\rm c}$, for $\Gamma = 2.6$, $\xi = 50$, $Z_{\rm Fe} = 9$, $i = 50°$, $\mathcal{R} = 1$, $a = 0.998$, $h_{\rm min} = 0$, and $r_{\rm in} = r_{\rm ISCO}$. The reflection spectra, shown by solid curves, correspond to $h_{\rm max} = r_{\rm c} = 1.3$ (black), 2 (red), 3 (green), 8 (blue), and 30 (magenta) from top to bottom. The primary spectrum is the same in all cases and is shown by the dashed line.

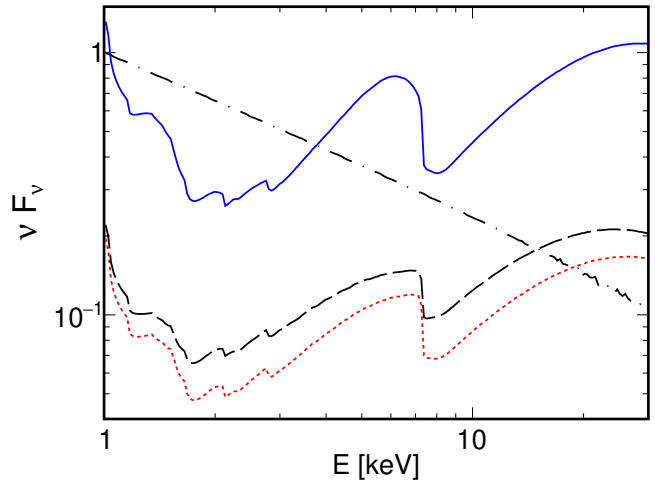

Fig. 2. Example illustration of the effect of the rotation of the X-ray source. The dotted red curve shows the reflection spectrum computed with `reflkerr_lp` (i.e. for a static point-like source, at $h = 2$.) The dashed black and solid blue curves show the reflection spectra computed with `reflkerr_elp` with $r_{\rm c} = 0.2$ and 1.5, respectively, in both $h_{\rm min} = h_{\rm hor}$ and $h_{\rm max} = 2$. In all three cases $\Gamma = 2.6$, $\xi = 50$, $A_{\rm Fe} = 9$, $i = 50°$, $a = 0.998$, $r_{\rm in} = r_{\rm ISCO}$ and $\mathcal{R} = 1$. The observed primary spectrum is the same in all three models and is shown by the dot-dashed black curve. The difference between the `reflkerr_lp` and the `reflkerr_elp` spectra is primarily due to the azimuthal motion of the emitting plasma in the latter, where $V \simeq 0.1$c for $r_{\rm c} = 0.2$ and $\simeq$0.8c for $r_{\rm c} = 1.5$.

from the combination of Doppler beaming and light bending. The latter effect is well known to increase the fraction of photons hitting the disc (Martocchia & Matt 1996), however, for a static source, the related enhancement of the observed reflection is rather weak (except for large i, see below). If the X-ray source rotates, its radiation is Doppler beamed to outer parts of the disc. Then, the observed reflection is not so strongly dependent on i. At the same time, the change of the irradiation profile resulting from the source rotation leads to a considerable change of the observed spectral shape of reflection.

Figure 2 illustrates the effect of azimuthal motion of the X-ray source; see also NZ08, who extensively studied the effects of the off-axis location of the X-ray source and its orbital motion. Our assumptions about co-rotation with the disc at $\rho \geq r_{\rm ISCO}$ and rigid rotation at $\rho < r_{\rm ISCO}$ appear to be natural and are the only choices that can be justified ab initio, unlike the unknown dynamics associated with magnetic flares. The angular velocity within $r_{\rm ISCO}$ in this model is equal to $\Omega_{\rm K}(r_{\rm ISCO})$, giving $V \simeq 0.1$c at $\rho = 0.2$, where V is the velocity measured in the locally non-rotating frame (Bardeen et al. 1972). At $h = 1.5$ and $\rho = 1.5$, $V \simeq 0.8$c is much larger than the Keplerian V in the equatorial plane. This is because V of a co-rotating source for a Kerr black hole increases with h at $h \lesssim \rho$ (see Sect. 2.2.3 in NZ08).

Figure 2 shows the results at $i = 50°$, relevant for 1H0707–495. For a static point-like source at $h = 2$, $\mathcal{R}_{\rm obs}/\mathcal{R}_{\rm obs,nr} \simeq 2$, although in this case $N_{\rm irr}/N_{\rm obs} \simeq 5$, where $\mathcal{R}_{\rm obs,nr}$ is the reflection strength for an isotropic source above a semi-infinite slab in flat space-time, and $N_{\rm irr}$ and $N_{\rm obs}$ are, respectively, the number of photons hitting the disc and observed directly from the source. This factor of 2 enhancement of the reflection strength is lower than the factor of 5 enhancement of the irradiating photon number compared to those observed as for a static lamppost; the enhanced irradiation occurs mostly at $r \lesssim h$ and the reflected radiation is directed mostly to large i (see e.g. Niedźwiecki & Zdziarski 2018), therefore, the related increase of $\mathcal{R}_{\rm obs}$ is rather modest for $i \lesssim 70°$.

The black dashed curve in Fig. 2 shows a mostly vertical extended source from the horizon that is $h_{\rm min} = h_{\rm hor}$ up to $h_{\rm max} = 2$, with very small radial extent $r_{\rm c} = 0.2$. This geometry is very similar to the lamppost for light bending but the rotation velocity of $V \simeq 0.1$c Doppler beams the radiation more towards the outer parts of the disc, where reflection gives a stronger contribution for small i and, hence, $\mathcal{R}_{\rm obs}$ is larger.

This effect is even more marked when the radial extent of the source is increased to $r_{\rm c} = 1.5$ because this has $V \simeq 0.8$c and $\mathcal{R}_{\rm obs}/\mathcal{R}_{\rm obs,nr} \simeq 15$. The increasing distortion of the reflection spectrum, as compared to the static source, is clearly seen.

Concluding the above discussion we note that significant changes of the angular distribution of radiation at the X-ray source (in particular, those related to the motion of the emitting plasma) may significantly change $\mathcal{R}_{\rm obs}$. However, they also lead to significant changes of the observed shape of the reflected spectrum owing to the change of the radial irradiation profile. Then, treating the reflection strength as a free parameter is unphysical and we again note that we scale it by $\mathcal{R}$ only to compare our results with earlier works. Models with $\mathcal{R} \gg 1$, such as found in Sects. 5.1 and 5.2, are clearly unphysical.

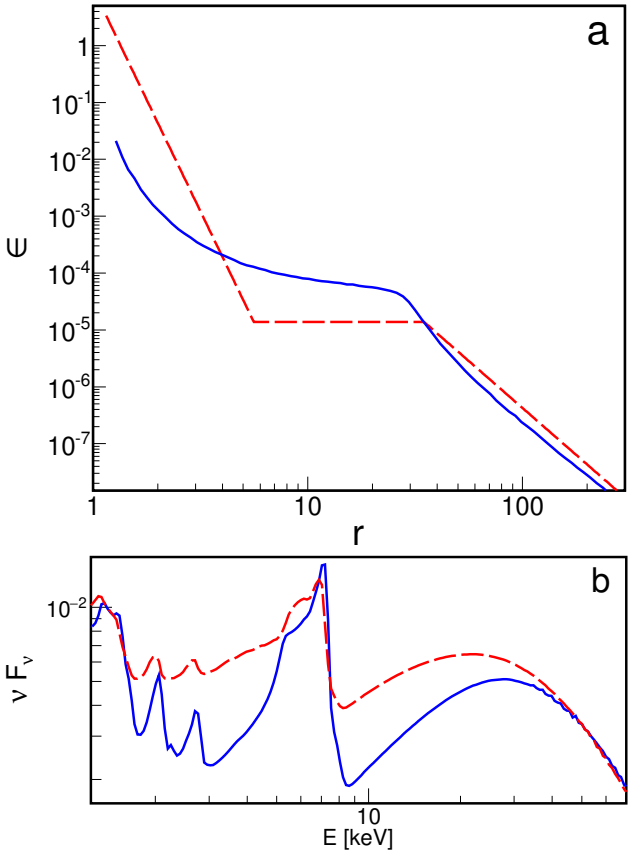

Fig. 3. *Panel a*: red line shows the twice-broken power-law, radial emissivity profile fitted to 1H0707–495 by Wilkins & Fabian (2011), see text. The blue line shows the emissivity profile produced by the X-ray source with $h_{\rm min} = 2$, $h_{\rm max} = 10$, $r_c = 30$, and $\Gamma = 3.1$. *Panel b*: reflection spectra for the emissivity profiles shown in panel a, and for $\Gamma = 3.1$, $\xi = 53$, $A_{\rm Fe} = 9$, $i = 54°$ and $r_{\rm in} = r_{\rm ISCO}$; the difference of spectral shapes is only due to different amounts of relativistic distortion corresponding to the difference of the radial profiles.

4. Comparison with empirical radial emissivity

The red curve in Fig. 3a shows the twice-broken power-law emissivity fitted to average spectra of 1H0707–495 by Wilkins & Fabian (2011), with the inner, middle, and outer indices of $q_1 = 7.8$, $q_2 = 0$, and $q_3 = 3.3$, respectively and the breaking radii of $r_{\rm br,1} = 5.6$ and $r_{\rm br,2} = 35$. In WF12, the authors argued that this inferred emissivity profile is consistent with that produced by an X-ray source with $r_{\rm c} \simeq r_{\rm br,2}$ (specifically, with $h_{\rm min} = 2$, $h_{\rm max} = 10$, and $r_{\rm c} = 30$). We use our code to explicitly calculate the emissivity of such an extended corona, shown by the blue curve in Fig. 3a. Our assumptions concerning the X-ray source are exactly the same as those of WF12 and our radial profile agrees with theirs (Fig. 15(b) in WF12). However, it differs substantially from the empirical profile of Wilkins & Fabian (2011). The empirical profile fitted to 1H0707–495 indicates a major contribution of radiation reflected from $r < 5$, which suffers strong redshift. However, while the irradiation profile produced by an extended source steepens at $r \lesssim 5$ (because of the blueshift of photons arriving at this region from X-rays produced in the corona at larger distances), this effect is too weak to reproduce the extremely steep (with $q \simeq 8$) inner part of the empirical profile. The contribution of reflection arising from $r < 5$ is only 15 per cent for the actual profile of an extended corona irradiating the disc, whereas it equals 97 per cent for the empirical profile.

Table 1. Results of spectral fitting of the coronal model `reflkerr` using empirical radial emissivities.

Model: `reflkerr`				
	VL	L	M	H
q_1	$-0.8^{+1.4}_{-\infty}$	$8.9^{+0.5}_{-0.6}$	$8.4^{+0.5}_{-0.4}$	$6.6^{+1.1}_{-0.9}$
q_2	$7.2^{+2.1}_{-1.1}$	$0.0^{+0.9}_{-0}$	$0.1^{+0.7}_{-0.1}$	$1.4^{+0.5}_{-0.8}$
q_3	–	$3.0^{+0.5}_{-0.4}$	$4.0^{+0}_{-0.7}$	$4.0^{+0}_{-0.6}$
$r_{\rm br,1}$	$2.3^{+0.3}_{-0.3}$	$4.5^{+0.5}_{-0.6}$	$5.0^{+0}_{-0.51}$	$4.7^{+0.3}_{-0.7}$
$r_{\rm br,2}$	–	$18.5^{+9.7}_{-5.6}$	$28.2^{+5.7}_{-5.7}$	$32.0^{+3.0}_{-9.1}$
Γ	$2.69^{+0.04}_{-0.16}$	$3.20^{+0.07}_{-0.07}$	$3.10^{+0.06}_{-0.03}$	$3.00^{+0.07}_{-0.03}$
ξ	$10^{+2.0}_{-0}$	$53.44^{(f)}$	$53.44^{(f)}$	$53.44^{(f)}$
$\mathcal{R}$	> 750	$88.2^{+20.4}_{-18.3}$	$29.1^{+5.1}_{-3.3}$	$11.4^{+3.1}_{-1.3}$
		χ^2/DoF		
(1)	119/86	290/132	293/141	347/140
(2)	173/127	836/688	1089/932	1123/950

Notes. The model fitted to L, M, and H assumes a twice-broken power-law, radial emissivity profile and $\xi = 53.44$. The model fitted to VL assumes a once-broken power-law profile; ξ is free. In all models $i = 53.96°$, and $Z_{\rm Fe} = 8.88$, $a = 0.998$, $r_{\rm in} = r_{\rm ISCO}$ and $r_{\rm out} = 1000$. The χ^2/DoF values correspond to spectral binning (1) and (2); see Sect. 2. The best-fit values and parameter uncertainties given in the table correspond to binning (1); the differences in the best-fit values obtained with binning (2) are insignificant. Quantity *(f)* denotes a fixed parameter. Following W14, for L, M, and H the fitted ranges of q_1, q_2, q_3, $r_{\rm br,1}$, and $r_{\rm br,2}$ are constrained to [5, 10], [0, 2], [2, 4], [3, 5], and [5, 35], respectively. The uncertainties are given for 90% confidence level. The uncertainties given as "+0" or "−0" correspond to the limit of the considered range of a parameter. The quantity ξ is given in units of erg cm s^{-1}.

The model matches well to the change in q seen a larger radii, from $q \simeq 0$ at $r \lesssim r_{\rm c}$ to $q \simeq 3$ at $r \gtrsim r_{\rm c}$. This is a simple geometrical effect that is also reproduced in flat space-time, however, it is of minor importance for the total reflection spectrum because so little of the total reflection signal is produced at these radii.

The large difference in emissivity from the central regions translates into a clear difference in predicted spectra, as shown in Fig. 3b. The extended corona of WF12 does not give the same reflected spectrum as derived from the empirical emissivity profile fit to the data from 1H0707–495.

5. Spectral analysis

In Sects. 5.1 and 5.2 we address W14, therefore, we follow their assumption that reflection is produced by weakly ionised disc and (still following W14) we adopt the Zoghbi et al. (2010) parameters of the reflection model as follows: ionisation parameter, ξ, iron abundance, $Z_{\rm Fe}$, and i. In Sect. 5.3 we relax these assumptions and allow a free fit of our extended corona model to the data.

5.1. Phenomenological radial emissivity

Following W14 we fitted the L, M, and H spectra assuming a twice-broken power-law, radial emissivity, for which we also adopted their constraints on the emissivity parameters (see the footnote of Table 1), and we fixed $\xi = 53.4$, $i = 53.96°$, $Z_{\rm Fe} = 8.88$, and $r_{\rm in} = r_{\rm ISCO}$. We applied model `reflkerr` (Niedźwiecki et al. 2019), which computes the reflection spectrum for an arbitrary twice-broken power-law, radial emissivity.

Our results, see Table 1, are consistent with those of W14. In particular, we find $r_{\rm br,2}$ between ≃20 and ≃30, increasing with the observed flux. The fit quality with spectral binning (2) is also consistent with W14 and seemingly excellent. For binning (1) we found only insignificant differences in the values of the fitted parameters, however, in this case they give a much worse $\chi^2/{\rm DoF} > 2$.

We now fit our extended disc corona reflection model directly to the data to explicitly test if this geometry can indeed produce the observed emissivity. The `reflkerr` model computes the transfer of both the reflected and direct radiation from the corona, therefore, properly calculates the reflection strength for this geometry. We find that the data can only be fit with an unphysically strong reflection component, namely $\mathcal{R} > 10$. This rules out the parameters of W14 for the disc-corona model in 1H0707–495. The empirical twice-broken power-law emissivity is only an approximation of models with a radially extended X-ray corona over the disc, and is a poor approximation for models with very steep inner emissivity as these produce much more inner disc reflection than is expected from an isotropic (in its rest frame), radially extended source.

For the VL spectrum, the twice-broken radial profile, with constraints on (q_1, q_2, q_3) of W14, does not give a good fit. We therefore fitted a single-broken profile (see Table 1). The fitted profile is very steep, having $q_2 > 7$ at $r > 2.3$. However, the inner $q_1 = -0.8$ indicates a strongly reduced contribution from $r \lesssim 2$. This break in the emissivity is highly significant. Using a single power law and setting $r_{\rm in} = r_{\rm ISCO}$ we get a much worse fit with $\Delta\chi^2 \simeq +50$ for binning (1). The fit also significantly improves after allowing ξ to vary; it then decreases to the minimum value allowed in `reflionx`, that is $\xi = 10$. The spectral feature observed in VL between ∼2 keV and ∼7 keV (see Fig. 4) can be reproduced by a relativistic line from a weakly ionised disc. However, in the disc-corona model such a spectral description requires an unrealistic reduction of the primary continuum, namely $\mathcal{R} > 750$ (see Fig. 5a), which again rules out this geometry.

5.2. Extended lamppost: plain reflection

We now use our model `reflkerr_elp`. We first aim to quantitatively test whether irradiation by an extended disc corona out to $r_{\rm c}$ can give a broken power-law emissivity with $r_{\rm c} \simeq r_{\rm br,2}$ as proposed by WF12 and W14. Therefore, (1) we keep the same assumptions about the rest-frame reflection as in the previous section, and (2) we set $r_{\rm c}$ equal to $r_{\rm br,2}$ of the `reflkerr` model fitted to a given state (Table 1). This gives much larger values of χ^2 than obtained with `reflkerr` in Sect. 5.1, specifically $\Delta\chi^2 \simeq (150–200)$ for spectra L, M, and H with binning (1) as shown in Table 2. There is no good fit for VL as discussed above, so we do not tabulate results for this spectrum.

The worsening of the fit shows that the disagreement between the empirical and physical emissivity profiles discussed in Sect. 4 is important even for the analysis limited to the 1–10 keV range. Using $r_{\rm br,2}$ to estimate r_c (as proposed by WF12 and W14) does not work for an extended corona geometry. The very large inner emissivities inferred from the twice-broken power law require a more radially concentrated X-ray illumination pattern than produced from a uniform corona, even in full general relativity.

This is the case even when we allow $r_{\rm c}$ to vary, rather than fixing it to $r_{\rm br,2}$. The inferred reflection in the data is dominated by the inner, extremely steep emissivity so the fitted $r_{\rm c}$ as well

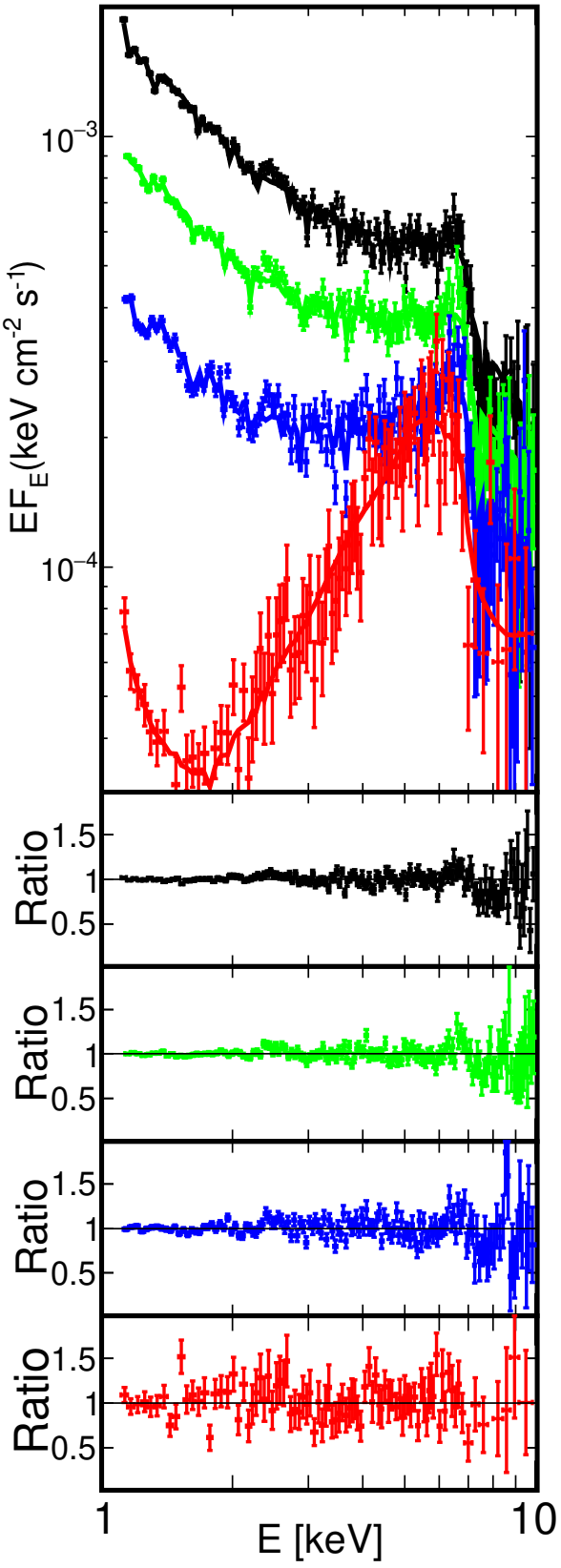

Fig. 4. *Top panel*: unfolded data and model spectra for our best-fitted models for VL (red), L (blue), M (green), and H (black) using `zxipcf*reflkerr_elp`. Spectral binning (1) was used. The model parameters are given in Table 4. The model is shown by the solid curve. *Bottom panel*: fit residuals given as the data-to-model ratio for VL, L, M, and H from bottom to top.

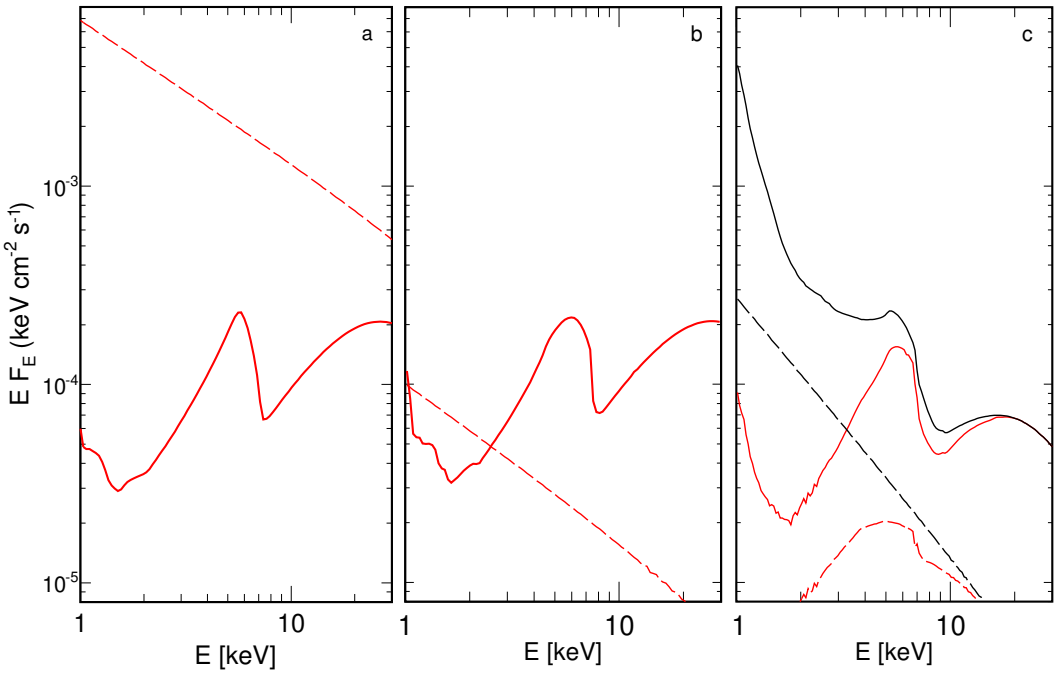

Fig. 5. Primary (dashed) and reflected (solid) spectra in our best models for VL with *panel a*: `reflkerr` (Sect. 5.1), *panel b*: `reflkerr_elp` with a weakly ionised disc (Sect. 5.2), and *panel c*: `reflkerr_elp` with a strongly ionised disc and an ionised absorber (Sect. 5.3). The spectra correspond to the fitted parameters for VL given in Tables 1, 3, and 4, respectively, except for $\mathcal{R}$, which was set to the physical value, i.e. $\mathcal{R} = 1$. As can be seen in Fig. 4, the observed VL spectrum has a strong depression at ∼2 keV. For the models shown in *panels a and b*, the contribution of the primary component must be artificially reduced by a factor >750 and >25, respectively, to obtain a similar spectral depression in the total spectra. In *panel c* the black curves show the unabsorbed and the red curves show the absorbed spectra. In this case, the relativistic effects combined with absorption allow us to reproduce the observed shape with $\mathcal{R} = 1$.

Table 2. Results of spectral fitting of the model `reflkerr_elp`, with r_c set to $r_{br,2}$ given in Table 1.

Model: `reflkerr_elp`			
	L	M	H
r_c	$18.5^{(f)}$	$28.2^{(f)}$	$32.0^{(f)}$
h_{max}	$35.5^{+10.2}_{-9.4}$	$26.1^{+8.4}_{-7.5}$	$12.4^{+6.5}_{-5.3}$
Γ	$2.52^{+0.02}_{-0.05}$	$2.69^{+0.02}_{-0.01}$	$2.84^{+0.01}_{-0.01}$
$\mathcal{R}$	$8.1^{+0.9}_{-0.6}$	$5.5^{+0.4}_{-0.4}$	$4.8^{+0.3}_{-0.5}$
	χ^2/DoF		
(1)	460/136	479/145	451/144
(2)	1057/692	1329/936	1348/954

Notes. In all models $a = 0.998$, $r_{out} = 1000$, $i = 53.96°$, $\xi = 53.44$, $Z_{Fe} = 8.88$, $r_{in} = r_{ISCO}$, and $h_{min} = 0$. The best-fit values and parameter uncertainties given in the table correspond to binning (1); the differences in the best-fit values with binning (2) are insignificant.

Table 3. Results of spectral fitting of our model `reflkerr_elp`.

Model: `reflkerr_elp`				
	VL	L	M	H
$r_c^{(a)}$	$1.5^{+0.1}_{-0.1}$	$0.1^{+0.3}_{-0}$	$0.1^{+0.5}_{-0}$	$0.3^{+0.6}_{-0.2}$
h_{max}	$1.5^{+0.3}_{-0.2}$	$2.4^{+0.2}_{-0.3}$	$2.4^{+0.4}_{-0.4}$	$3.0^{+0.8}_{-0.6}$
Γ	$2.77^{+0.04}_{-0.15}$	$3.09^{+0.07}_{-0.10}$	$3.01^{+0.06}_{-0.03}$	$3.00^{+0.02}_{-0.03}$
ξ	$10^{+2.6}_{-0}$	53.44^{f}	53.44^{f}	53.44^{f}
$\mathcal{R}$	> 25	$10.7^{+2.2}_{-2.4}$	$3.9^{+0.5}_{-1.2}$	$2.5^{+0.4}_{-1.7}$
r_{in}	$1.7^{+0.2}_{-0.1}$	$r_{ISCO}^{(f)}$	$r_{ISCO}^{(f)}$	$r_{ISCO}^{(f)}$
	χ^2/DoF			
(1)	119/86	314/135	313/144	353/143
(2)	183/128	859/691	1113/935	1129/953

Notes. In all models $a = 0.998$, $r_{out} = 1000$, $i = 53.96°$, and $Z_{Fe} = 8.88$; $h_{min} = 0$ in VL and $h_{min} = r_{hor}$ in L, M, and H. The best-fit values and parameter uncertainties given in the table correspond to binning (1); the differences in the best-fit values with binning (2) are insignificant. $^{(a)}$ The minimum value of r_c allowed in the `reflkerr_elp` model is 0.1.

as h_{max} are very small for all spectra, as detailed in Table 3. This means that the source geometry is now close to that of the standard lamppost, except that it is rotating.

For such small r_c and h_{max}, any value of h_{min} between r_{hor} and h_{max} gives identical results because radiation from h close to h_{max} dominates both the observed and irradiating flux. For simplicity, for all results presented in this section, we assumed $h_{min} = r_{hor}$ for L, M, and H. For VL, where the fitted r_c is slightly larger, we assumed $h_{min} = 0$; allowing h_{min} to vary does not change the results.

Figure 6 shows the probability distributions and correlations between r_c, h_{max} and $\mathcal{R}$, obtained using the Markov chain Monte Carlo (MCMC) method. The major degeneracy concerns the anti-correlation between r_c and $\mathcal{R}$ in L, M, and H, which is related to the increase of V with r_c (for the assumed velocity field close to the symmetry axis, see Sect. 3). This is due to the increase of reflection strength with V (see Fig. 2). The VL spectrum requires a negligible contribution of the primary component, namely $\mathcal{R} \gtrsim 25$, see Fig. 5b, so for this state we do not get the $\mathcal{R} - r_c$ anti-correlation.

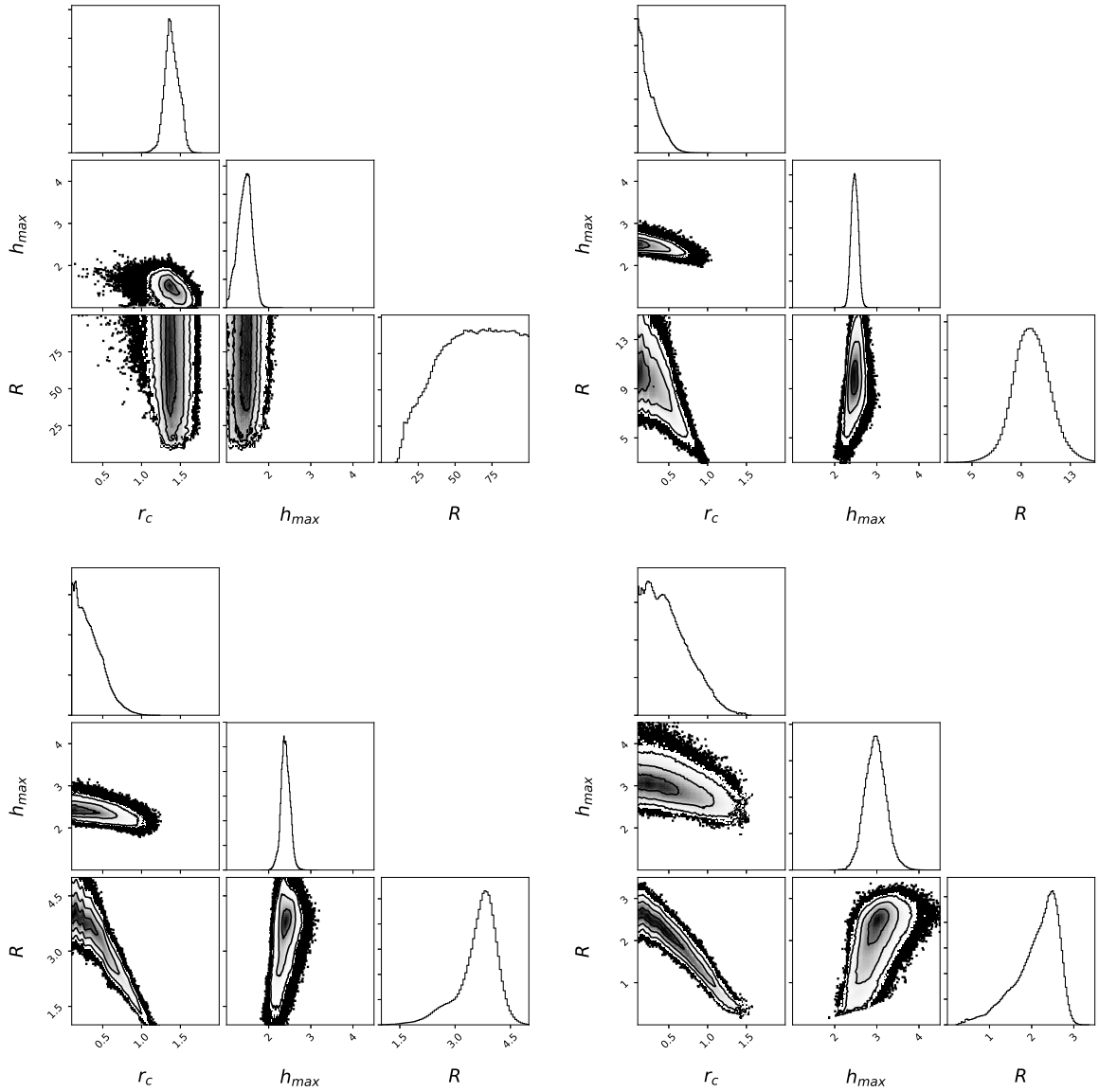

Fig. 6. Probability distributions showing correlations between the r_c, h_{max}, and $\mathcal{R}$ parameters of the `reflkerr_elp` model with a weakly ionised disc (see Table 3) fitted in the 1.1–10 keV range to the VL (*top left*), L (*top right*), M (*bottom left*), and H (*bottom right*) spectrum, obtained in the MCMC analysis using `xspec_emcee` implemented by Jeremy Sanders. The results of this analysis are presented using package `corner` (Foreman-Mackey 2016). The contours in the 2D plots correspond to the significance of $\sigma = 1, 2, 3$. The histograms show the probability distributions for the individual parameters.

For VL we also allowed $r_{\rm in}$ to vary and we find that $r_{\rm in} > r_{\rm ISCO}$ is formally significant; setting $r_{\rm in} = r_{\rm ISCO}$ gives, for binning (1), $\Delta\chi^2 = 17$.

All these fits are somewhat worse than those of the phenomenological broken power-law emissivity reflection fits, typically by $\Delta\chi^2 \sim 10$–20 for binning (1). This is because the model geometry is now reproducing the inner, very steep emissivity, where most of the reflection signal is produced, at the expense of the weak outer reflection component. More concerning is that they all require $\mathcal{R} > 1$ so are physically unrealistic except for the brightest state (H).

The pure reflection models clearly show that the best-fit, extended source geometry is not very extended for all the spectra of 1H0707–495. The illumination pattern derived from these fits requires a very centrally concentrated X-ray corona, close to the lamppost geometry except for its rotation kinematics modifying the illumination pattern. Hence there is also no evidence that the size of the corona is correlated with the luminosity, as claimed in W14.

5.3. Extended lamppost: reflection and ionised absorption

We now include photo-ionised absorption in addition to our model for reflection from the extended disc-corona, `reflkerr_elp`, as multiple studies have shown that this is significantly present (Dauser et al. 2012; Hagino et al. 2016; Kosec et al. 2018). We first model this absorption using the `zxipcf` model implemented in `xspec`, although we note that this assumes only a rather small turbulent velocity broadening of 200 km s^{-1}, that is much smaller than those inferred from the data (around 10 0000 km s^{-1} in Kosec et al. 2018). This model also assumes solar abundances for all elements, whereas the reflection fits typically require large overabundance of iron and uses an ion population calculated assuming $\Gamma = 2.2$, which is

Table 4. Results of spectral fitting of the model `reflkerr_elp`, with a partially covering ionised absorption computed with `zxipcf`.

Model: `zxipcf*reflkerr_elp`				
	VL	L	M	H
		`zxipcf`		
n_H	17^{+2}_{-2}	113^{+69}_{-73}	51^{+42}_{-36}	23^{+31}_{-14}
$\log_{10}(\xi)$	$1.6^{+0.9}_{-0.3}$	$3.9^{+0.2}_{-0.4}$	$4.0^{+0.1}_{-0.2}$	$3.9^{+0.1}_{-0.4}$
$f_{\rm cov}$	$0.98^{+0.01}_{-0.01}$	$1.0^{+0}_{-0.13}$	$1.0^{+0}_{-0.16}$	$1.0^{+0}_{-0.45}$
z	$0.04^{+0}_{-0.03}$	$-0.09^{+0.01}_{-0.01}$	$-0.10^{+0.01}_{-0.01}$	$-0.12^{+0.01}_{-0.01}$
		`reflkerr_elp`		
$r_{\rm c}$	$1.7^{+0.5}_{-0.4}$	$1.1^{+0.1}_{-0.1}$	$0.6^{+0.1}_{-0.2}$	$0.7^{+2.2}_{-0.6}$
$h_{\rm max}$	$1.8^{+1.1}_{-1.2}$	$3.8^{+1.3}_{-0.4}$	$4.0^{+0.5}_{-0.6}$	$4.8^{+1.0}_{-0.9}$
i [°]		$39.7^{+0.9}_{-1.3}$		
$Z_{\rm Fe}$		$5.0^{+0.4}_{-0.3}$		
Γ	$3.27^{+0.03}_{-0.17}$	$2.38^{+0.02}_{-0.02}$	$2.55^{+0.01}_{-0.01}$	$2.68^{+0.01}_{-0.01}$
ξ	5010^{+2140}_{-2690}	1050^{+110}_{-60}	2120^{+180}_{-300}	3850^{+920}_{-510}
$\mathcal{R}$	> 0.6	$1.4^{+1.0}_{-0.3}$	$1.5^{+1.2}_{-0.1}$	$1.0^{+0.1}_{-0.2}$
$r_{\rm in}$	$2.6^{-0.5}_{-0.5}$	$1.4^{+0.5}_{-0.2}$	$1.4^{+0.2}_{-0.2}$	$1.3^{+0.2}_{-0.1}$
		χ^2/DoF		
(1)		671/484		
	92	202	182	196
(2)		2841/2682		
	146	742	977	976

Notes. Negative values of the redshift parameter in `zxipcf` give the blueshift corresponding to an outflow of the absorber. In all models $a = 0.998$ and $r_{\rm out} = 1000$; $h_{\rm min} = 0$ in VL and $h_{\rm min} = r_{\rm hor}$ in L, M, and H. The model is fitted jointly to the four states with linked i and $Z_{\rm Fe}$. We give χ^2/DoF for the joint fit and contribution of individual states to the total χ^2. The best-fit values and parameter uncertainties given in the table correspond to binning (1); the differences in the best-fit values with binning (2) are negligible. n_H is given in the unit of 10^{22} cm^{-2}.

rather harder than that inferred for 1H0707–495. Nonetheless, it gives a simple model to approximately characterize some of the spectral complexity associated with partially ionised absorption.

We do not impose any constraints on the model parameters except for linking the reflection i and $Z_{\rm Fe}$ across all four states, and fixing $a = 0.998$. The spectral fitting results are given in Table 4, Fig. 4 shows the spectra and best-fit models to all states.

Adding the photo-ionised absorber significantly improves the spectral description in all four states, both compared to the extended disc-corona fits with free corona size shown above, and even compared to the phenomenological twice-broken power-law emissivity fits. We allow here the scaling parameter of reflection, $\mathcal{R}$, to vary but all fits correspond to a physically self-consistent $\mathcal{R} \simeq 1$. This is even the case for the VL spectrum, which always previously required $\mathcal{R} \gg 1$.

Figure 5 shows the sequence of model fits to the VL spectrum, with the direct power law (dashed) and reflection component (solid) shown separately. Panel a shows the low-ionisation `reflkerr` fit with reflection calculated from the phenomenological emissivity as in Sect. 5.1, but for a reflection normalisation set to the physical $\mathcal{R} = 1$ rather than the extreme values required from the fits. Even though the emissivity best fit is a single, very centrally concentrated power law, gravitational effects alone are not sufficient to enhance the reflection to the extent required by the data. Panel b shows the fit with reflection calculated from the self-consistent illumination pattern of an extended, rotating corona. The disc ionisation parameter is similarly low to that derived from the phenomenological emissivity fits. Thus the reflected component shape is much the same, but its amplitude is now dramatically enhanced by the source kinematics, with the intrinsic rotation changing the illumination pattern on the disc. However, this is still insufficient to explain the inflection in the VL data at 2 keV. Instead, panel c shows the fit including ionised absorption. Unlike the L, M, and H fits, the ionised absorber in VL is only moderately rather than highly ionised ($\xi \sim 40$ rather than 10^4). Its effect on the spectrum is to produce strong continuum curvature rather than distinct ionised absorption line features, with a strong low-energy cut-off below 4 keV from bound-free transitions in metals such as Si, S, and Fe L. This continuum curvature gives a much better fit to the data and changes the shape of the best-fit reflection spectrum so that it now is better described by a highly ionised disc. This increases the amount of reflection at low energies compared to the Compton hump and shifts the line thereby shifting the line and edge energies. The total continuum spectrum then has a strong dip at 2 keV as well as at 9 keV, as observed in the data (see also Fig. 4).

Figure 4 also shows the other datasets fit with this model including ionised absorption. The change in behaviour of the continuum at low energies between VL and L, M, and H is obvious; L, M and H instead give the best-fit ionised absorption, which is highly ionised $\xi \sim 10^4$.

For all the datasets, the geometry of the extended source is changed very little from that derived in the previous section. Both $r_{\rm c}$ and $h_{\rm max}$ are small, making the model much more like a lamppost (but with rotation) than a corona with a large-scale extent over the disc. Similar to Sect. 5.2, we assume $h_{\rm min} = r_{\rm hor}$ for L, M, and H and $h_{\rm min} = 0$ for VL; allowing $h_{\rm min}$ to vary does not change our results.

However, despite the lack of change in source geometry, all the spectral fits are now consistent with $\mathcal{R} \simeq 1$. This is because of the much larger inferred ionisation state of the reflector, with $\xi > 1000$, in all four states instead of $\xi = 10$–60 in fits without the additional ionised absorption. The disc albedo is strongly enhanced by ionisation, which enhances the reflection spectrum in soft X-rays for the same radial and vertical extent of the X-ray source.

The ionised absorber in L, M, and H is highly ionised; therefore this absorber has little continuum absorption and is instead dominated by ionised line features. The inferred columns are extremely high, with $N_h \sim 1.1 \times 10^{24}$ cm^{-2} for L, which is optically thick to electron scattering. The inferred columns for M and H are lower, but only by a factor 2-5. Scattering of the continuum from the ionised absorbing material must be important at these columns, so the model is not self-consistent. These derived columns could be overestimated as they depend strongly on the velocity structure of the absorbing material. Absorption lines saturate when the core of the line becomes optically thick, that is when photons at the line centre cannot escape at the rest energy of the transition. Increasing the column beyond this cannot lead to much more absorption as there are no more photons at the line centre to remove. Absorption increases in the wings of the line, but Doppler wings are very steep so the line equivalent width does not increase much as the column increases. A larger spread of velocity in the absorbing material gives a wider but shallower line for the same column, so it remains optically thin at higher columns. Fits to 1H0707–495 by Kosec et al. (2018) indicate that the velocity width of the line is around 13 000 km s^{-1} as opposed to the 200 km s^{-1} used in `zxipcf`, which reduces the columns to around 2–4×10^{23} cm^{-2}. However, this still has an optical depth

to electron scattering of ~0.2. The geometry of the material then determines how much the scattered emission contributes to the spectrum, and it is not just scattered continuum but also resonance line scattering. Calculating the contribution of these cannot be done analytically for non-spherical geometries, rather this requires a Monte Carlo radiation transfer code.

5.4. Disc reflection and wind absorption and scattering

We apply the Monte Carlo radiation transport code `monaco` (Odaka et al. 2011) to model the absorption and scattering self-consistently from a bipolar wind geometry (Hagino et al. 2015, 2016, 2017; Tomaru et al. 2018). We use the specific bipolar wind simulation of Mizumoto et al. (2019), which is tailored to fit to the time average spectrum of 1H0707–495 (similar to the M and H spectra used here). The model assumes a black-hole mass of $2 \times 10^6\, M_\odot$, with a wind filling an axi-symmetric bicone between 45−56.3° (so that the solid angle from the focal point d below the black hole is $\Omega/2\pi = 0.15$), launched at $d = r_{\rm min} = 50$, corresponding to an escape velocity of 0.2c. The mass-loss rate in the wind is set to $\dot{M}_{\rm wind}/\dot{M}_{\rm Edd} = 0.2$ and this, combined with the velocity law, gives the density structure along the wind streamlines. This is illuminated by a power law with $\Gamma = 2.6$ and $L_{\rm X} = 0.003 L_{\rm Edd}$ to get the self-consistent ionisation structure. Mizumoto et al. (2019) show that the scattered spectrum in this simulation can also account for the time lags seen in this source around the iron line energy.

We now use this combined absorption and scattering wind model to modify the intrinsic emission and its reflection from the disc. We model the latter via `reflkerr` with a phenomenological emissivity fixed to a single power law with $q = 3$. This is justified because after adding the wind component we find that the inner radius of the reflecting material increases to a very large value, implying only a very mild relativistic distortion of the reflected spectrum. The fits now have to be restricted to energies above 2 keV due to the energy band limitations of the tabulated model.

We could not get a good fit for the VL spectrum, as we no longer include the less ionised material (probably clumps within the wind), which produces the very marked spectral curvature in these data. These less ionised clumps are probably still present in L, M, and H, but at a lower level (smaller covering fraction, see Hagino et al. 2016) so the spectrum can be fit without including this material. Hagino et al. (2016) show that the brightest, steepest spectra are least affected by these clumps, so we plot the best fit for H in Fig. 7. All parameters are given in Table 5, but the reduced energy range means that the goodness of fit cannot be directly compared with previous models. Hence we also refit the `zxipcf*reflkerr_elp` model to the same energy range; the χ^2/DoF for the joint fit to L, M, and H (with linked i and $Z_{\rm Fe}$) is 369/326 for binning (1). Hence the fit with the wind model is somewhat worse in terms of $\Delta\chi^2$, but the number of degrees of freedom in the model are also lower because it is computed only for a single fixed wind geometry.

Including the scattered emission from the wind dramatically changes the requirement for reflection from the disc to be distorted by extreme relativistic effects. However, the model is still not self-consistent as the inferred amount of reflection from the disc is strongly enhanced over that expected, with $\mathcal{R} \sim 6$ rather than $\simeq$1. Imposing the constraint of $\mathcal{R} = 1$, we find that small values of both the inner radius of the disc and the source size are again required. The model also has very different assumptions about metallicity, namely $Z_{\rm Fe} = 5$ is fitted for the reflector, compared to solar in the wind.

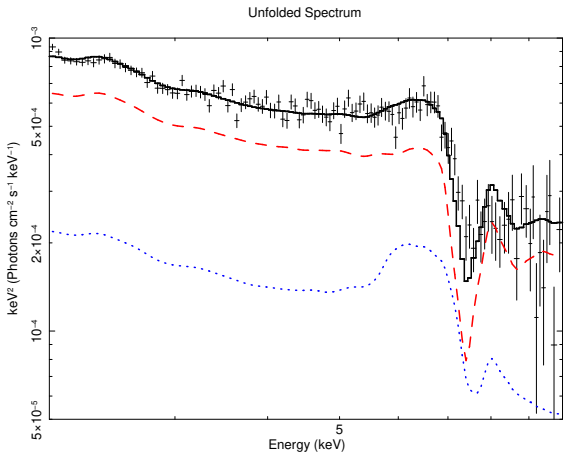

Fig. 7. Unfolded data and model spectrum for our best-fitted model for H using `monaco*reflkerr`. The red curve shows the total (i.e. primary power law + reflection) transmitted component attenuated by absorption. The blue curve shows the total scattered component.

Table 5. Results of spectral fitting in the 2–10 keV range of the model `reflkerr`, with wind absorption and scattering computed with `monaco`.

Model: `monaco*reflkerr`			
	L	M	H
$r_{\rm in}^{(a)}$	$770^{+\infty}_{-485}$	$718^{+\infty}_{-538}$	$755^{+\infty}_{-587}$
i [°]		$61.1^{+0.2}_{-2.7}$	
$Z_{\rm Fe}$		$5.3^{+1.7}_{-0.4}$	
Γ	$2.31^{+0.03}_{-0.03}$	$2.61^{+0.03}_{-0.03}$	$2.78^{+0.02}_{-0.03}$
ξ	210^{+20}_{-20}	498^{+7}_{-100}	520^{+50}_{-50}
$\mathcal{R}$	$7.3^{+1.6}_{-1.3}$	$6.3^{+0.9}_{-0.8}$	$6.3^{+0.7}_{-1.2}$
		χ^2/DoF	
(1)		509/344	
	159	176	174
(2)		2142/2028	
	553	765	825

Notes. In all models $q = 3, a = 0.998$ and $r_{\rm out} = 1000$. `monaco` was computed for a fixed wind geometry and the same inclination angles are assumed for the disc and wind, so this component does not add any free parameters in our fitting procedure. The model is fitted jointly to the three states with linked i and $Z_{\rm Fe}$. We give χ^2/DoF for the joint fit and contribution of individual states to the total χ^2. The best-fit values and parameter uncertainties given in the table correspond to binning (1); the differences in the best-fit values with binning (2) are negligible. $^{(a)}$ Symbol "+∞" denotes $r_{\rm in}$ approaching $r_{\rm out} = 1000$.

6. Summary

This paper shows the model of reflection from an extended corona geometry, which can be directly fit to X-ray spectral data. All previous models assumed either a point-like source (lamppost) or some phenomenological radial emissivity. The authors of WF12 associated a twice-broken power-law emissivity with the illumination pattern expected from a uniform extended corona, with the outer break indicating the radial extent of the corona, a uniform illumination interior to this, and then a marked enhancement at small radii due to light bending and other GR effects. However, we show that this qualitative match to extended corona models is not a good quantitative fit to real data. We use 1H0707–495 as apparently the most extreme relativistic reflection source, and directly fit it with both a twice-broken

power-law phenomenological emissivity and the full illumination pattern produced by an extended disc corona. The outer break radius of the emissivity, $r_{\rm br,2} \sim 30$, so according to WF12 indicates a corona of size $r_{\rm c} = 30$. Explicitly fitting a uniform extended corona with $r_{\rm c} = 30$ to the data produces a reflection spectrum that strongly deviates from that observed for any scale height because the self-consistent, centrally peaked illumination pattern is not as steep as required by the phenomenological fits.

Instead, allowing the size (as well as the height) of the corona to be a free parameter makes the corona collapse in size. The best-fit corona geometry derived from these fits to the data is a very compact source of $\lesssim 1R_{\rm g}$ in size, and is located at most $\sim 2R_{\rm g}$ from the black-hole horizon in all flux states. These fits show a corona that is highly centrally peaked, rather than uniformly extended. This is close to the original lamppost model used initially for computational convenience, although we also point out the importance of the source rotation in our model, which makes a large increase in the amount of relativistic reflection that escapes to infinity.

The fitted location of the X-ray source is interestingly consistent with that estimated previously by fitting the lamppost model to the time-averaged (Dauser et al. 2012) and time-dependent (Caballero-García et al. 2018) spectra in 1H0707–495, which in both cases gives $h \simeq 3$. The latter, however, depends on the black-hole mass, and the lamppost model of Caballero-García et al. (2018) cannot explain the measured delay spectra if it is $5.3 \times 10^6\, M_\odot$ (Pan et al. 2016) rather than $2 \times 10^6\, M_\odot$ estimated in earlier works.

In our analysis we considered only a fixed, maximum value of black-hole spin, $a = 0.998$. Such a high value was estimated in the lamppost model by Dauser et al. (2012) and the fitted values of the inner radius of the disc, $(1.3{-}1.4)R_{\rm g}$ (Sect. 5.3) indicate that $a > 0.99$ is required in this version of the model.

We do not find any sizable changes of the corona geometry between different X-ray flux levels, which would lead to varying distortion of the reflection component, such as shown in Fig. 1. The spectral variations appear to be mostly from the change of both the amplitude and slope of the primary emission spectrum and the change of the disc ionisation state. We note some hints of geometrical changes only for a VL state, with a weak truncation of the disc at about $2R_{\rm g}$ (which is ruled out at higher states) and a weak decrease of the height and increase of the radius. However, the large difference between this VL and higher flux spectra is primarily due to the difference of the ionisation state of the absorber.

Our fits then strongly favour a compact source on the spin axis of the black hole. Yet it is difficult to produce a physical model of such a source. There are strong limits on the amount of X-rays that could be produced by Comptonisation of disc photons (Dovčiak & Done 2016), and the radiative efficiency is strongly reduced owing to photon trapping by the black hole (Niedźwiecki et al. 2016).

Including the effect of simple models of ionised absorption from the wind (see also Dauser et al. 2012; Kosec et al. 2018) does not change the conclusions about the source size fit to the data, but does indicate that these models are not self-consistent because the large columns of ionised material inferred contribute substantially to the spectrum via electron scattering and line emission and resonance line scattering. We use the specific bipolar wind Monte Carlo calculation of Mizumoto et al. (2019) and find that the inclusion of the scattered flux from the wind can dramatically change the parameters. With this model, the reflection spectrum from the disc is only mildly distorted by relativistic effects, and indicates the disc extending down to $700R_{\rm g}$ only, rather than requiring most of the reflection to come from within $5R_{\rm g}$; the fit however is somewhat worse than for the phenomenological absorption only models.

Nonetheless, even this model is incomplete as the inferred amount of reflection from the disc is much larger than expected in this geometry, and the metallicities of the reflector and wind are different, and most importantly, we neglect any additional absorption from clumps of less ionised material entrained in the hot wind. While such winds cannot be easily modelled ab initio, they may hold the key to the dramatic spectral features seen in the most extreme active galactic nuclei.

Acknowledgements. We thank Andrzej Zdziarski and the referee, Thomas Dauser, for valuable comments. This research has been supported in part by the Polish National Science Centre grants 2014/13/B/ST9/00570, 2015/18/A/ST9/00746 and 2016/21/B/ST9/02388. A. N. is a member of the International Team 458 at the International Space Science Institute (ISSI), Bern, Switzerland, and thanks ISSI for the support during the meeting in Bern. M. M. acknowledges support from Japan Society for the Promotion of Science (JSPS) overseas research fellowship and Hakubi project at Kyoto University.

References

Bardeen, J. M., Press, W. H., & Teukolsky, S. A. 1972, ApJ, 178, 347
Boller, T., Fabian, A. C., Sunyaev, R., et al. 2002, MNRAS, 329, L1
Brenneman, L. 2013, Measuring the Angular Momentum of Supermassive Black Holes (Springer)
Caballero-García, M. D., Papadakis, I. E., Dovčiak, M., et al. 2018, MNRAS, 480, 2650
Dauser, T., Svoboda, J., Schartel, N., et al. 2012, MNRAS, 422, 1914
Dauser, T., Garcia, J., Parker, M. L., Fabian, A. C., & Wilms, J. 2014, MNRAS, 444, L100
Done, C., & Jin, C. 2016, MNRAS, 460, 1716
Done, C., Sobolewska, M. A., Gierliński, M., & Schurch, N. J. 2007, MNRAS, 374, L15
Dovčiak, M., & Done, C. 2016, Astron. Nachr., 337, 441
Fabian, A. C., & Ross, R. R. 2010, Space Sci. Rev., 157, 167
Fabian, A. C., Zoghbi, A., Ross, R. R., et al. 2009, Nature, 459, 540
Fabian, A. C., Zoghbi, A., Wilkins, D., et al. 2012, MNRAS, 419, 116
Foreman-Mackey, D. 2016, J. Open Source Softw., 24
Hagino, K., Odaka, H., Done, C., et al. 2015, MNRAS, 446, 663
Hagino, K., Odaka, H., Done, C., et al. 2016, MNRAS, 461, 3954
Hagino, K., Done, C., Odaka, H., Watanabe, S., & Takahashi, T. 2017, MNRAS, 468, 1442
Jansen, F., Lumb, D., Altieri, B., et al. 2001, A&A, 365, L1
Kosec, P., Buisson, D. J. K., Parker, M. L., et al. 2018, MNRAS, 481, 947
Laor, A. 1991, ApJ, 376, 90
Laor, A., Netzer, H., & Piran, T. 1990, MNRAS, 242, 560
Martocchia, A., & Matt, G. 1996, MNRAS, 282, L53
Miniutti, G., & Fabian, A. C. 2004, MNRAS, 349, 1435
Mizumoto, M., Ebisawa, K., Tsujimoto, M., et al. 2019, MNRAS, 482, 5316
Niedźwiecki, A., & Życki, P. T. 2008, MNRAS, 386, 759
Niedźwiecki, A., & Miyakawa, T. 2010, A&A, 509, A22
Niedźwiecki, A., & Zdziarski, A. A. 2018, MNRAS, 477, 4269
Niedźwiecki, A., Zdziarski, A. A., & Szanecki, M. 2016, ApJ, 821, L1
Niedźwiecki, A., Szanecki, M., & Zdziarski, A. A. 2019, MNRAS, 485, 2942
Odaka, H., Aharonian, F., Watanabe, S., et al. 2011, ApJ, 740, 103
Pan, H.-W., Yuan, W., Yao, S., et al. 2016, ApJ, 819, L19
Reynolds, C. S., & Begelman, M. C. 1997, ApJ, 488, 109
Reynolds, C. S., Young, A. J., Begelman, M. C., & Fabian, A. C. 1999, ApJ, 514, 164
Ross, R. R., & Fabian, A. C. 2005, MNRAS, 358, 211
Ruszkowski, M. 2000, MNRAS, 315, 1
Strüder, L., Briel, U., Dennerl, K., et al. 2001, A&A, 365, L18
Suebsuwong, T., Malzac, J., Jourdain, E., & Marcowith, A. 2006, A&A, 453, 773
Tanaka, Y., Nandra, K., Fabian, A. C., et al. 1995, Nature, 375, 659
Tanaka, Y., Boller, T., Gallo, L., Keil, R., & Ueda, Y. 2004, PASJ, 56, L9
Tomaru, R., Done, C., Odaka, H., Watanabe, S., & Takahashi, T. 2018, MNRAS, 476, 1776
Wilkins, D. R., & Fabian, A. C. 2011, MNRAS, 414, 1269
Wilkins, D. R., & Fabian, A. C. 2012, MNRAS, 424, 1284
Wilkins, D. R., Kara, E., Fabian, A. C., & Gallo, L. C. 2014, MNRAS, 443, 2746
Zoghbi, A., Fabian, A. C., Uttley, P., et al. 2010, MNRAS, 401, 2419

Appendix A: `reflkerr_elp`

The construction of the `reflkerr_elp` model[3] closely follows that of `reflkerr_lp`. In particular, the convolution of the general-relativistic effects with the rest-frame radiation spectra makes use of the transfer functions; these transfer functions, following Laor et al. (1990) and Laor (1991), are constructed by tabulating a large number of photon trajectories. The transfer functions are computed only for a single value of the spin parameter, $a = 0.998$. The source-to-disc and source-to-observer transfer functions are tabulated in a grid including 51 bins in both ρ and h. We use 50 bins logarithmically spaced between $\rho = 0.1$ and 50, and the additional bin for $\rho = [0, 0.1]$, and similarly 50 bins logarithmically spaced between $h = 0.1$ and 50, and the additional bin for $h = [0, 0.1]$. Then, in our parametrisation of the model, both the r_c and h_{max} parameters can be fitted in the range of $[0.1, 50]$. To compute these transfer functions, we generated photon trajectories sampling the region at $0 \leq h \leq 50$ and $0 \leq \rho \leq 50$ with uniform probability density; at each point the initial direction in the source rest frame was generated with an isotropic probability distribution. The photon trajectories were computed via the code developed by NZ08. For the disc-to-observer transfer we use the same transfer functions as in `reflkerr` and `reflkerr_lp`.

Our model relies on the numerical accuracy of the code of NZ08, therefore, we now briefly compare this code with other similar computations. Irradiation of an accretion disc by a single point-like source, located off the symmetry axis of the Kerr metric, has been considered in a number of works, many of which are aimed at explaining some observed variability effects by the change of the location of the source (e.g. Reynolds et al. 1999; Ruszkowski 2000; Miniutti & Fabian 2004; Niedźwiecki & Miyakawa 2010; NZ08). There were some differences in the interpretation of the reduced variations of the reflected component in the model with a co-rotating source, which effect was attributed to light bending by Miniutti & Fabian (2004), whereas NZ08 clarified that it is mostly due to the assumed dependence of the source rotation velocity on its height. However, the quantitative results of these studies, for example the dependence of the reflection strength (typically represented by the Fe line flux in these works) on the source location, were in fairly good agreement.

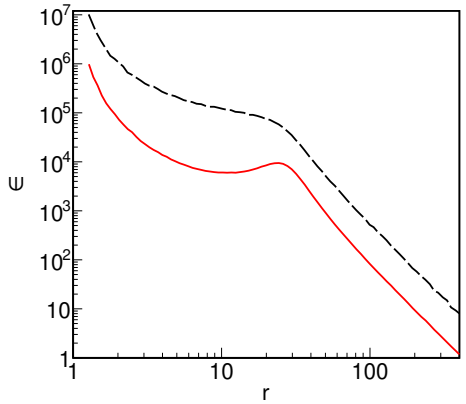

Fig. A.1. Radial emissivity profiles for a point-like and an extended source, to be compared with Fig. 10 in WF12. The dashed black curve is for a disc-like source with $h = 10$ and $\rho \leq 25$. The red solid curve is for a point-like source at $h = 10$ and $\rho = 25$.

Suebsuwong et al. (2006) and NZ08 show radial profiles for disc irradiation, which can be compared to those presented by WF12, and again there seems to be a good agreement between these three works. In Fig. A.1 we show the emissivity profiles, computed with the code of NZ08, in the form suitable for the comparison with Fig. 10 in WF12. We see that the profiles computed with these two codes match very well. The same was found for the case of the extended corona (Fig. 3a) and we note again that the difference between the conclusions of our work and that of Wilkins et al. do not result from any differences between the computational models, but from the different methods of their application to data interpretation.

[3] The model can be downloaded at `https://users.camk.edu.pl/mitsza/reflkerr_elp`